

Effects of extratropical warming on ENSO amplitudes in an ensemble of a coupled GCM

Kuniko Yamazaki · Masahiro Watanabe

Received: 7 August 2013 / Accepted: 15 April 2014 / Published online: 1 May 2014
© The Author(s) 2014. This article is published with open access at Springerlink.com

Abstract The El Niño-Southern Oscillation (ENSO) amplitudes in an ensemble of twentieth-century coupled general circulation model experiments performed for the Coupled Model Intercomparison Project phase 5 were found to have a systematic relationship with the time-averaged Southern Ocean sea surface temperature (SST). That is, the ENSO amplitudes were greater in the ensemble members with warmer Southern Ocean SST. Here we propose a mechanism that explains how the anomalous extratropical warming remotely affects the ENSO strength. First, the reduction in the meridional temperature gradient over the Southern Hemisphere gives rise to an anomalous northward heat transport by transient eddies across the extratropics into the tropics. This induces an anomalous Hadley cell that leads to a northward heat transport within the tropics in its upper branch and a southward moisture transport in the lower branch. The latter reduces maximum precipitation in the intertropical convergence zone in the equatorial Pacific Ocean and increases precipitation in the adjacent region to the south. Since the amount of precipitation over the eastern equatorial Pacific dictates the strength of ENSO through the shift in the zonal wind stress response to El Niño/La Niña, we conclude that there is an energy transport pathway through which the ENSO strength can be remotely modulated by the anomalous heating in the extratropics.

Keywords El Niño-southern oscillation · ITCZ · Atmospheric energy transport

K. Yamazaki (✉) · M. Watanabe
Atmosphere and Ocean Research Institute,
The University of Tokyo, 5-1-5 Kashiwanoha,
Kashiwa-shi, Chiba 277-8564, Japan
e-mail: kuniko@aori.u-tokyo.ac.jp

1 Introduction

It is widely recognized that the El Niño-Southern Oscillation (ENSO) phenomena impact regional climate in various parts of the world (Ropelewski and Halpert 1987, 1989; Halpert and Ropelewski 1992). As global climate warms under increasing greenhouse gas concentrations, mean climate in the tropical Pacific Ocean, where the ENSO events occur, is expected to change, with probable repercussions on the ENSO variability (Collins et al. 2010). Considering the immensity of the worldwide socio-economic impact these changes may impart, meaningful predictions of ENSO events are doubtlessly of vital importance.

The ENSO amplitude is defined as the variability in the sea surface temperature (SST) anomaly from the climatological mean state in the pre-defined regions (e.g. Niño-3 and 4 regions) in the equatorial Pacific Ocean. It is often used to quantify the mean ENSO “strength”. Representations of present-day ENSO amplitudes in general circulation models (GCMs) in Coupled Model Intercomparison Project phase 5 (CMIP5; Taylor et al. 2012) have improved in the majority of the GCMs when compared with those simulated in phase 3 (CMIP3; Meehl et al. 2007), but discrepancies still exist among the different GCMs (Guilyardi et al. 2012; Bellenger et al. 2013). Such discrepancies likely result from the biases among the GCMs in the mean climate state of the equatorial Pacific as well as in a number of physical processes and feedbacks that control the ENSO. Collins et al. (2010) conclude that how ENSO will change under global warming is uncertain at this stage because we do not yet know the collective effect of the altered physical processes and feedbacks, and propose that “a reliable projection model for ENSO” consistent with current theoretical understanding and observational records

be produced. As a small step forward, we aim to identify in this study a cause of the diversity in the ENSO amplitudes in a historical ensemble of one of the CMIP5 coupled GCMs, the Model for Interdisciplinary Research on Climate (MIROC5; Watanabe et al. 2010). The five-member MIROC5 historical ensemble displays a rather large range of ENSO amplitudes spanning more than half of that given by the entire CMIP5 multi-model ensemble. Furthermore, the ENSO amplitudes in the MIROC5 ensemble evince a systematic relationship with the area-mean SST in the Southern Hemisphere (SH) extratropics. In this paper we aim to ascertain whether this relationship is physically meaningful and, if so, to identify the underlying mechanism that bridges the two seemingly remote phenomena.

One possibility is through the process of precipitation. Mean precipitation in the eastern-equatorial Pacific is known to measure well the ENSO amplitude due to mutual interaction (Watanabe et al. 2012). That is, the mean state affects the ENSO via different wind stress responses to SST anomaly and, conversely, the ENSO affects the mean state via precipitation asymmetry with respect to the ENSO phase (Watanabe et al. 2012). If there is a remote physical process acting between the SH extratropical SST and the eastern-equatorial Pacific mean precipitation, it may explain the relationship exhibited in the MIROC5 historical ensemble.

One such remote process has been brought to attention by recent findings on the meridional shift of the inter-tropical convergence zone (ITCZ), a long belt of intensive convection and hence precipitation in the deep tropics. Studies involving paleoclimate records from periods with asymmetric interhemispheric ice cover, and climate simulations using a variety of structurally different GCMs with asymmetric north–south warming or cooling, provide mounting evidence that the ITCZ moves towards the warmed hemisphere (e.g. Chiang and Bitz 2005; Broccoli et al. 2006; Yoshimori and Broccoli 2009; Kang et al. 2008, 2009, 2011; Frierson and Hwang 2012; Su et al. 2008). These studies point to the change in the Hadley circulation as a cause of the change in the ITCZ location. Kang et al. (2008, 2009), in particular, suggest that (in their case, imposed) extraneous extratropical heat flux is balanced by inter-hemispheric changes in the atmospheric heat transport by transient eddies in the extratropics and by the Hadley circulation in the tropics, and by local changes mainly in the cloud radiative feedback. The change in the Hadley circulation can also be instigated by global warming through an increase in static stability due to the warming of the upper troposphere (Mitas and Clement 2006; Lu et al. 2007; Gastineau et al. 2008). Studies based on coupled GCMs with a dynamic ocean model also attribute ocean processes in the equatorward transport of extraneous extratropical heat, albeit at longer timescales

(Su et al. 2008; Menviel et al. 2010). Su et al. (2008) also find changes in the zonal shift of the ITCZ that accompany changes in the Walker circulation. This shift in the ITCZ, and hence in the precipitation amount in the equatorial region, caused by extraneous heat in the extratropics, may explain the relationship between the ENSO amplitude and the extratropical SST found in the MIROC5 historical ensemble, on which this study will focus.

The paper is structured as follows. The model used in this study and the experiment design within the CMIP5 framework are outlined in Sect. 2. Section 3 highlights the characteristics of ENSO and the Southern Ocean warming observed in the model results. In Sect. 4 we analyze key model diagnostics and discuss their association with the extratropical warming. Summary and discussion are given in Sect. 5.

2 Model and experiment

The primary data used in this study are results from climate simulations using MIROC5 coupled atmosphere–dynamic ocean GCM (Watanabe et al. 2010). The model's atmosphere component has a resolution of T85 in the horizontal and 40 levels in the vertical. The ocean component is the version 4.5 of the CCSR Ocean Component Model (COCO; Hasumi 2006). The zonal resolution is 1.4° everywhere; the meridional resolution is 1.4° poleward of 8N and 8S and 0.5° at lower latitudes. There are 49 levels in the vertical, with finer resolution towards the surface. The MIROC5 data used in this study consist of a long, single model run in the pre-industrial control experiment (hereafter CTL) and a five-member ensemble of runs in the historical experiment (hereafter 20C), all performed as a part of the CMIP5. CTL was externally forced with a fixed pre-industrial radiative forcing with the seasonal cycle and was run for 670 model years. The 20C runs were initiated from climate states in CTL taken at different timepoints, and were run under radiative forcing conditions from 1850 to 2005. We have made use of 566 model years of the CTL, from the branch-off timepoint of r5i1p1 to 156 years after the branch-off timepoint of r1i1p1. This allowed us to match each member of the 20C ensemble with a corresponding CTL period.

3 Model climatology

3.1 Model ENSO

Figure 1 shows the ENSO amplitudes in the Niño-3 region (5S–5N, 150W–90W) in observational data (HadISST; Rayner et al. 2003), the MIROC5 20C ensemble, the

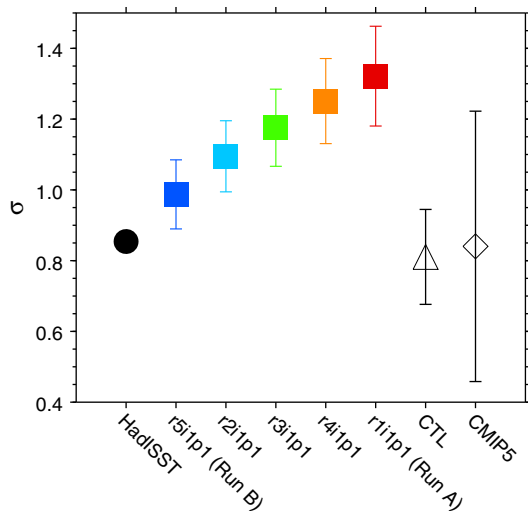


Fig. 1 Standard deviation σ of Niño-3 area-averaged SSTA derived from various datasets. Colored squares, a filled black circle, a triangle and a diamond denote the 20C ensemble, the HadISST observational dataset, CTL and the CMIP5 multi-model ensemble, respectively. In 20C, HadISST and CMIP5 σ was computed over the years 1940–1999 and in CTL over the entire 566-year period. Colors correspond to the degree of the warming of the Southern Ocean SST in each 20C ensemble member, from blue being the coolest to red being the warmest. Error bars for the 20C ensemble (CTL experiment) were assessed from a set of σ computed in 60-year (156-year) subsets, which were generated by repeatedly shifting the years included in the subset forward by 1 year along the time axis. The error bar for CMIP5 is the range of σ defined by 17 different GCMs

MIROC5 CTL run and the CMIP5 multi-model ensemble taken from the coupled-model historical experiment. The list of models from the CMIP5 are shown in Table 1. The amplitude is represented by σ , the standard deviation of the area-weighted mean SST anomaly (SSTA) in the Niño-3 region. In the 20C ensemble (denoted by colored squares in Fig. 1) σ shows a spread of 0.33 ± 0.12 K. In CTL, σ has a range of 0.27 K, which is an estimate of the model’s internal variability. The spread of σ among the members of the 20C ensemble is therefore greater than the maximum range of σ arising from the model’s internal variability, and thus we can dismiss the null hypothesis that the diversity of the former has occurred by chance.

The observed present-day (black circle) and the mean CMIP5 (diamond) ENSO amplitudes are both slightly smaller than those simulated in 20C. The range of 20C ENSO amplitudes roughly fall in the upper half of the range displayed by the GCMs in CMIP5. (Although the 20C runs are included in the CMIP5 dataset, the maximum σ in the 20C runs exceeds the upper limit of the CMIP5 range in Fig. 1. This is due to the differences in the horizontal resolution of the SST data used to compute σ . The CMIP5 data were uniformly converted to $2.5^\circ \times 2.5^\circ$.)

As mentioned earlier, the 20C ensemble consists of five members, which are labeled in the CMIP5 data archive as

Table 1 Models used in the analyses of this study

Model name	Climate modeling group
BCC-CSM1.1	Beijing Climate Center, China Meteorological Administration
CanESM2	Canadian Centre for Climate Modelling and Analysis
CCSM4	National Center for Atmospheric Research
CNRM-CM5	Centre National de Recherches Météorologiques/ Centre Européen de Recherche et Formation Avancéee Calcul Scientifique
CSIRO-Mk3.6.0	Commonwealth Scientific and Industrial Research Organization in collaboration with Queensland Climate Change Centre of Excellence
GFDL-CM3	NOAA Geophysical Fluid Dynamics Laboratory
GISS-E2-H	NASA Goddard Institute for Space Studies
GISS-E2-R	NASA Goddard Institute for Space Studies
HadCM3	Met Office Hadley Centre
HadGEM2	Met Office Hadley Centre
INM	Institute for Numerical Mathematics
IPSL-CM5A-LR	Institut Pierre-Simon Laplace
IPSL-CM5A-MR	Institut Pierre-Simon Laplace
MIROC5	Atmosphere and Ocean Research Institute (The University of Tokyo), National Institute for Environmental Studies, and Japan Agency for Marine-Earth Science and Technology
MPI-ESM-LR	Max Planck Institute for Meteorology
MRI-CGCM3	Meteorological Research Institute
NorESM1-M	Norwegian Climate Centre

Table 2 Descriptions of 20C ensemble members

Run name in CMIP5	Year of initial state branch-off from CTL	Mean southern ocean SST (C ·)	σ (K)
r5i1p1	20	3.75 ± 0.05	0.99 ± 0.10
r2i1p1	80	3.91 ± 0.05	1.09 ± 0.10
r3i1p1	180	4.01 ± 0.05	1.17 ± 0.11
r4i1p1	280	4.09 ± 0.03	1.25 ± 0.12
r1i1p1	410	4.19 ± 0.03	1.32 ± 0.14
piControl	–	3.84 ± 0.05	0.81 ± 0.13

Time and area-weighted average of Southern Ocean SST were taken over years 1940–1999 and over 80S–50S, respectively. σ is the standard deviation of the area-weighted mean SSTA calculated over years 1940–1999 with respect to 1961–1990 average over the Niño-3 region. Ranges were assessed from a set of values of each variable computed in 60-year subsets, which were generated by repeatedly shifting the years included in the subset forward by 1 year along the time axis. Ranges for CTL were assessed from 156-year subsets

$mi1p1$ (where $n = 1, 2, \dots, 5$). Table 2 shows the list of properties relating to the five 20C members and the CTL. For the purpose of clarity, in this paper we focus on the two

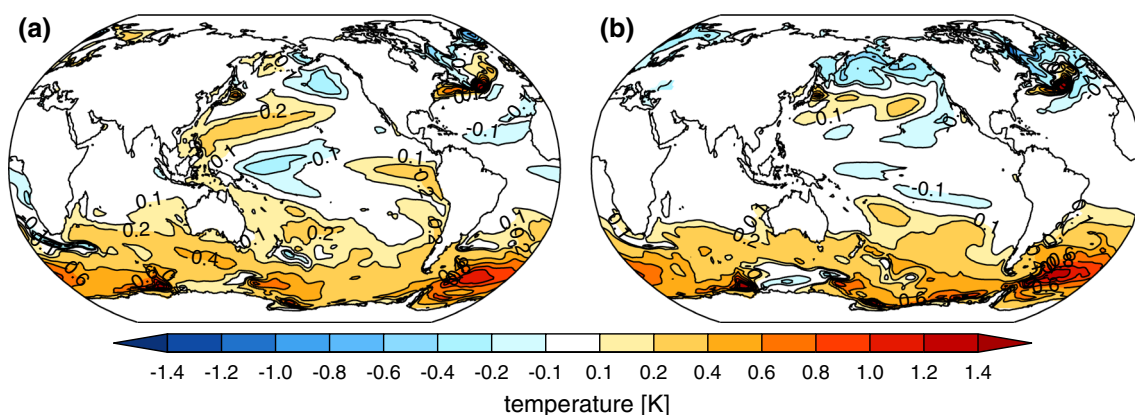


Fig. 2 Time-mean SST difference between **a** 20C Run A and Run B and **b** CTL Epoch A and Epoch B

members r1i1p1 and r5i1p1 and hereafter refer to them as Run A and Run B. They are the two ends of the range in σ , mean Southern Ocean SST and the branch-off time from CTL. Furthermore, we extract two 156-year-long sections from CTL that start from the timepoints at which the initial conditions for Run A and Run B had been taken. We refer to these sections as Epoch A and Epoch B. Epoch A (Epoch B) is expected to be identical to Run A (Run B), except for the external forcing used in their simulations.

It is noted that CTL has climate drift, which is still a common problem among the CMIP5 models (Gupta et al. 2013). In CTL the global volume-mean ocean temperature increases steadily throughout the experiment under a positive top-of-the-atmosphere (TOA) radiative imbalance with a 566-year average value of 0.68 Wm^{-2} . This is reflected in the fact that the 20C ensemble members initiated from the CTL climate states at later timepoints exhibit larger mean Southern Ocean SST, as shown in Table 2.

3.2 Extratropical warming

Figure 2 shows the time-mean SST difference between (a) Run A and Run B in the 20C experiment and (b) Epoch A and Epoch B in the CTL experiment. A significant warming is apparent in the Southern Ocean in both experiments. The geographical patterns of warming in the two experiments are very similar. A greater amount of warming in the equatorial Pacific in (a) may reflect stronger ENSO in the 20C runs compared with CTL, as seen in Fig. 1. In order to quantify the effect of the Southern Ocean SST difference on the rest of the globe, we examine the difference in the atmospheric energy budget over 50S–90S between Run A and Run B. We seek to measure the extent to which the extraneous heat into the region is dealt with locally in the form of the difference in the radiative feedbacks and how much is exported to the lower latitudes via the atmospheric circulation or into land or the ocean. The

exchange of atmospheric energy will occur at the three boundaries: at the top of the atmosphere (TOA), at the vertical wall at 50S and at the surface. If radiative forcing Q is imposed at TOA,

$$Q = H + R_T \quad (1)$$

where H is the upward radiative flux out of TOA into space (Gregory and Mitchell 1997) and R_T is the net downward radiation at TOA. H can be broken down into radiative feedbacks, e.g. that due to the basic radiative balance (Planck feedback), the water–vapor greenhouse forcing, the total cloud radiative forcing and the surface albedo effect (given in terms of clear-sky net downward shortwave radiation; Gregory and Mitchell 1997; Klingaman 2009).

The net downward radiation at TOA, R_T , will be taken up by the atmosphere and the surface, the latter of which is predominantly the ocean. Combining the thermodynamic equation and the moisture conservation and vertically integrating through the atmosphere column, and further assuming the tendency terms are small by considering the annual mean, we obtain the following relationship,

$$\nabla \cdot F_A = R_T - F_s \quad (2)$$

where

$$F_A = \frac{1}{g} \int_0^{p_s} h v dp \quad (3)$$

is the atmospheric energy transport, g is acceleration due to gravity, p_s is surface pressure, h is moist static energy (MSE), v is velocity and p is pressure (Trenberth and Solomon 1994). If we integrate Eq. (2) zonally, we obtain the meridional energy flux out of the vertical wall.

We now examine the differences in the surface air temperature and the respective components of the atmospheric energy budget between Run A and Run B. The energy budget will be evaluated at TOA, across the vertical

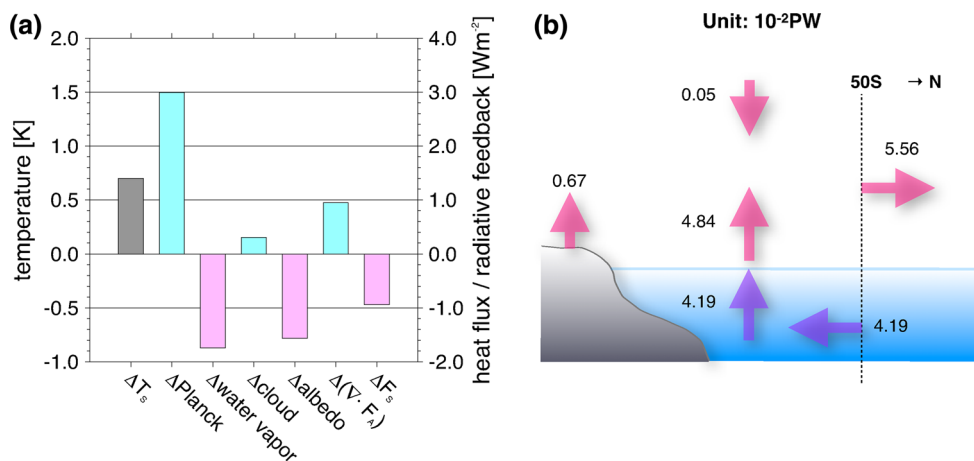


Fig. 3 **a** Area-weighted mean, time-mean differences between Run A and Run B in temperature, radiative forcing and energy fluxes averaged over 50S–90S. *Bars from left* indicate differences in the surface air temperature, Planck feedback, clear-sky water–vapor greenhouse forcing, total cloud radiative forcing, TOA clear-sky shortwave forcing (effect of change in surface albedo), net radiative flux into the atmosphere and net radiative flux into land and ocean, respectively. Outgoing fluxes from the atmosphere in the 50S–90S region are defined positive; therefore the atmosphere in this region is

cooled more or warmed less in Run A than in Run B by the fluxes colored in cyan. The converse is indicated for the fluxes colored in pink. Individual terms were computed offline as shown in the “Appendix”. **b** Budget of energy transport difference between Run A and Run B. The discrepancy between the surface energy flux difference given by the ocean ($4.19 \times 10^{-2} PW$) and that received by the atmosphere ($4.84 \times 10^{-2} PW$) arises from the off-line grid conversion between atmosphere and ocean data

wall at 50S and at the surface. As the tendency over the 156 years of the 20C experiment is similar among the ensemble members, we can define Δ to express the difference in the time-mean values between Run A and Run B. Figure 3a shows the surface air temperature, radiative feedbacks and energy fluxes in the 50S–90S region, given as differences between Run A and Run B. The individual terms were calculated offline as shown in the “Appendix”. Outgoing fluxes from the atmosphere in the 50S–90S region are defined positive. The positive difference in the surface air temperature, ΔT_s , also evident in Fig. 2a, is consistent with an increase in the loss of heat to space, as clearly shown in the positive difference in the Planck feedback. Forcing due to the water vapor feedback warms Run A more than it does Run B, whilst that due to total cloud radiative forcing cools Run A more than Run B. There is more cooling of the atmosphere in the region in Run A by total cloud radiative forcing ($0.3 Wm^{-2}$), which is broken down into more cooling by the cloud shortwave forcing ($0.62 Wm^{-2}$) and more warming by the cloud longwave forcing ($-0.32 Wm^{-2}$). This indicates an increase in the amount of the low or high clouds and in the amount or the height of the high clouds. The clear-sky shortwave forcing into the region is increased in Run A due to a reduction in sea ice and hence in surface albedo.

Area-averaged surface flux F_s over 50S–90S is negative in both runs (-8.05 and $-7.13 Wm^{-2}$ in Run A and Run B, respectively), which indicates that the atmosphere is heated by the ocean. This is primarily because the ocean

surface in this region is warmer on average than the overlying atmosphere. The difference ΔF_s is negative, which implies that in this region more energy is transported into the atmosphere from the land/ocean surfaces in Run A than in Run B. In contrast, $\Delta(\nabla \cdot F_A)$ is positive, which indicates that a greater amount of atmospheric energy is exported from the region in Run A than in Run B via the change in the atmospheric circulation.

In Fig. 3b a schematic diagram highlights the differences in the energy transport between Run A and Run B across regions/ model components. The atmospheric and oceanic vertical fluxes were calculated from either TOA or surface fluxes from the atmospheric and oceanic model diagnostics, respectively, the atmospheric meridional flux is F_A , and the oceanic meridional flux was output directly as an ocean model diagnostic. It shows that in the region poleward of 50S, a greater amount of energy in Run A than in Run B is imported across 50S into the Southern Ocean by the ocean circulation ($4.193 \times 10^{-2} PW$), and then transported from the ocean to the atmosphere through the surface energy exchange ($\Delta F_{s-A} = -4.194 \times 10^{-2} PW$, where A is sea surface area south of 50S). There is a discrepancy of about 15 % between this flux and that received by the atmosphere ($4.838 \times 10^{-2} PW$); the discrepancy arises from the off-line grid conversion between atmosphere and ocean data values. The energy is then exported across 50S to the northern latitudes by the atmospheric circulation ($\Delta(\nabla \cdot F_A) = 5.56 \times 10^{-2} PW$, where F_A is zonally integrated) to compensate for the poleward ocean heat transport.

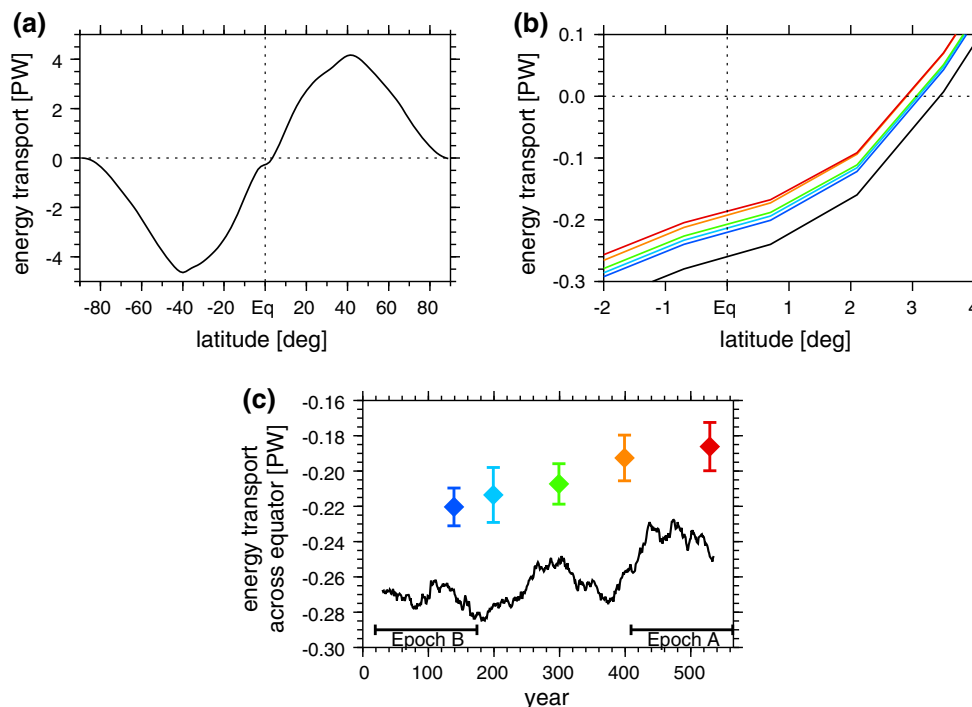


Fig. 4 **a** Time mean, zonally-integrated meridional energy transport F_A for CTL over Epoch B. **b** A close-up of **(a)** in the vicinity of the equator, overplotted with the corresponding curves for the 20C ensemble averaged over the years 1940–1999. **c** *Connected black dots* indicate 60-year mean values of the zonally-integrated meridional energy transport at the equator for CTL. The x -coordinate of each dot corresponds to the midpoint of the averaging period. *Colored diamonds* denote the values at the equator of the colored curves in

(b). The x -coordinate of each diamond indicates the midpoint of the averaging period, which starts from the beginning of the period in CTL. *Colors* correspond to the degree of the warming of the Southern Ocean SST in each 20C ensemble member, from *blue* being the coolest to *red* being the warmest. *Error bars* were assessed from a set of mean F_A computed in 60-year subsets, which were generated by repeatedly shifting the years included in the subset forward by 1 year along the time axis

To summarize, in the MIROC5 20C ensemble, warmer southern high-latitudes correlates with stronger ENSO and increased northward meridional energy transport by the atmospheric circulation. In the next section, we investigate whether this relationship is physically meaningful.

4 Effects of extratropical warming

In the previous section, we identified a relationship that exists between the anomalously warm extratropical SST and the change in the meridional atmospheric energy transport. In this section we examine the latter closely.

4.1 Meridional energy transport

4.1.1 Total moist static energy

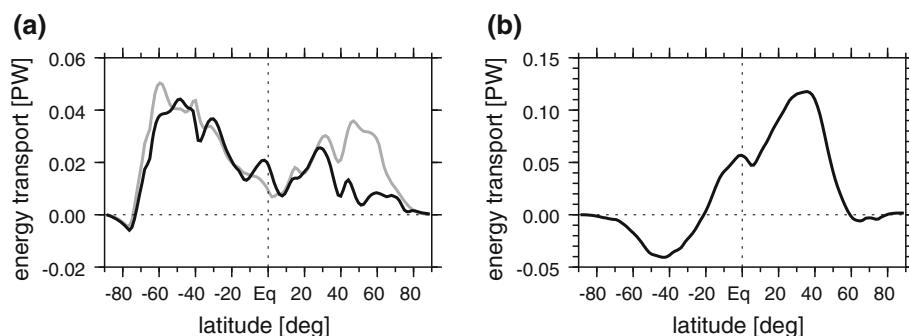
Here we examine the meridional atmospheric energy transport F_A by zonally integrating Eq. (3). Figure 4a shows a typical latitude-dependence curve of annual mean F_A . The transport is defined positive northwards; at the equator F_A is slightly negative and the latitude at which F_A

changes sign is approximately 3N. This means that in the annual mean, the poleward energy transport inverts its direction not at the equator but slightly to the north. This latitude can be interpreted as an approximate boundary between the two annually averaged Hadley cells. At the boundary the large latent heat convergence combined with strong ascending motions due to diabatic heating induces strong cumulus convection leading to heavy rainfall; therefore this latitude is also the approximate position of the zonal mean ITCZ.

Figure 4b shows a close-up of the curve in Fig. 4a in the vicinity of the equator, overplotted with the corresponding curves for the 20C ensemble averaged over the years 1940–1999. It is clearly shown that the warmer the extratropical SST, the weaker the cross-equatorial energy flux and the more southward the zero-crossing latitude of F_A . This is in agreement with the findings in other studies reviewed in Sect. 1 that report the southward shift of the ITCZ towards the warmed hemisphere.

Figure 4c displays the evolution of the cross-equatorial energy transport with time. Two features beg attention. First, compared with CTL, the amount of energy transported by the 20C ensemble members is systematically

Fig. 5 Differences in time mean, zonally-integrated meridional energy transport F_A . Differences are between **a** Run A and Run B (black line) and Epoch A and Epoch B (gray line) and **b** 20C ensemble mean and CTL mean. Unit is petawatts



less. The only imposed difference between CTL and 20C is the external forcing, so this marked difference in the northward energy transport is likely to have arisen from the disparate pre-industrial and twentieth-century external forcing. We shall henceforth call this source of the difference the “external forcing” component. Second, the cross-equatorial energy transport in CTL and 20C have the common tendency to decrease with time (in the case of 20C, to decrease with the points in time at which the initial conditions for the 20C experiments were extracted from CTL.) This implies that the northward energy transport is affected by the model’s climate drift.

Figure 5 illustrates the sources of the difference found in F_A among individual runs/experiments. The second, “remote forcing” component of the source of the difference, arising from the warmer southern extratropical SST, is exemplified in Fig. 5a as the difference between Run A and Run B (black curve). A large peak around 60S clearly shows the extraneous energy from the warmer Southern Ocean being transported northward. The gray curve shows the difference in F_A between the corresponding periods in the CTL, i.e. between Epoch A and Epoch B. The two curves are overall quite similar, with small discrepancies northward of 40N and at the equator. The similarity in the shape and magnitude of the two curves indicates that the component of F_A associated with the “remote forcing” component was present in the CTL run and has been imparted to the 20C ensemble via the initial conditions.

Figure 5b shows the difference in the meridional MSE transport between the 20C ensemble mean and the CTL mean, illustrating the “external forcing” component in Fig. 5a. As the amount in Fig. 5b is positive between 22S and 58N, the 20C “external forcing” component has the effect of increasing the absolute northward transport (see Fig. 4a) between 3N and 58N. Conversely, the absolute southward transport is decreased between 3N and 22S and increased to the south of 22S. These differences reflect on the differences in the 20C and CTL SST (not shown). Namely, compared with CTL, 20C SST is cooler in the Northern Hemisphere (NH), with a minimum at approximately 40N, due to the higher levels of aerosol forcing, and

is warmer in the subtropical region in both hemispheres. This has the effect of increasing the equator-to-subpolar temperature gradient in the NH whilst reducing that in the Southern Hemisphere (SH). The temperature gradient between the SH subtropics and the South Pole is increased, however; hence the increase in the southward energy transport to the south of 22S.

4.1.2 MSE transport by transient eddies

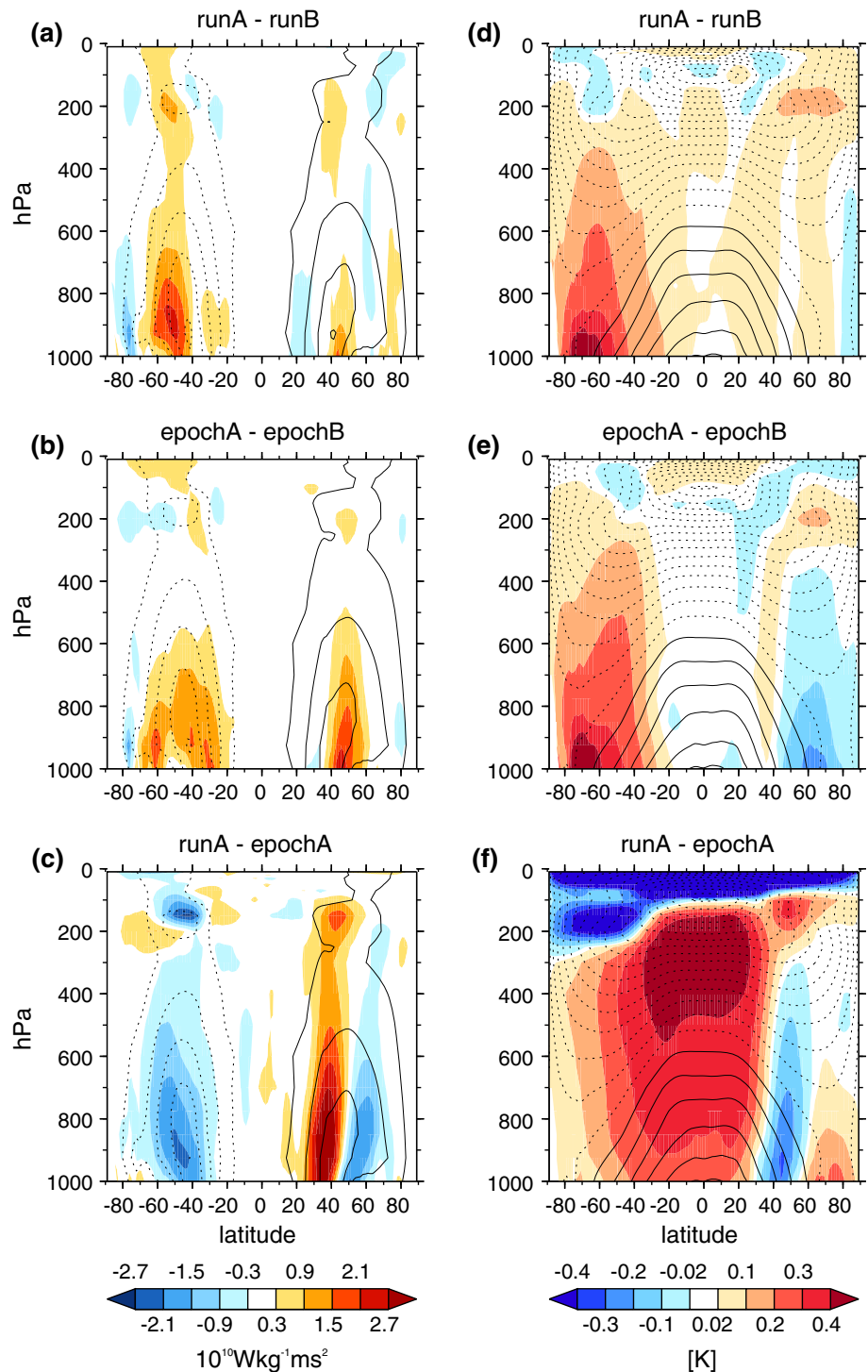
The meridional transport of MSE, vh , in Eq. (3) can be broken down into sensible heat, potential energy and latent heat, as follows

$$vh = c_p vT + gvz + L_v vq \tag{4}$$

where c_p is specific heat of dry air at constant pressure, T is temperature, z is geopotential height, L_v is latent heat of evaporation and q is specific humidity. When taking the time and zonal means, each element of the MSE transport can be decomposed into transports by different dynamical processes. The sensible heat transport, for example, is expressed as $c_p [\overline{vT}] = c_p [\overline{v}] [\overline{T}] + c_p [\overline{v'T'^*}] + c_p [\overline{v'T'']}$, where overbars and square brackets denote time and zonal means, respectively, and ' and * denote deviations therefrom, respectively. The terms on the right hand side indicate sensible heat transport by the mean meridional circulation, the stationary eddies and the transient eddies, respectively (Peixoto and Oort 1991).

Figure 6a–c show vertical sections of the time-mean, zonally-integrated meridional transport of MSE by transient eddies. The transport is positive in NH (solid lines) and negative in SH (dotted lines). The color-filled contours indicate the differences of the transport between runs and/or epochs. If we assume that the effects of the “remote forcing” and “external forcing” components combine linearly when they are superimposed, we should be able to separate out the effect of the “remote forcing” by taking the difference between Run A and Run B (or Epoch A and Epoch B), as shown in Fig. 6a, b, and the effect of the “external forcing” by taking the difference between Run A and Epoch A as shown in Fig. 6c. In Fig. 6a, there is a

Fig. 6 Vertical sections of time-mean, zonally-integrated meridional MSE transport by transient eddies (*left column*) and time-mean, zonal-mean temperature (*right column*). Solid and dotted lines denote the positive and negative absolute values of Run B (*top*), Epoch B (*middle*) and Epoch A (*bottom*), respectively. Colors denote the differences between Run A and Run B (*top*), Epoch A and Epoch B (*middle*) and Run A and Epoch A (*bottom*), respectively. The fields are averaged over the years 1940–1999. Contour intervals are 2×10^{11} (*left*) and 5 (*right*). Unit is $\text{Wkg}^{-1} \text{ms}^2$ (**a–c**), degrees Celsius (**d–f lines**) and K (**d–f colors**)



distinct region of positive MSE transport difference at 40S–70S. In SH the positive difference between Run A and Run B implies reduced transport in Run A due to the “remote forcing” component.

Figure 6d–f show vertical sections of time-mean, zonal-mean temperature. Each panel corresponds to that for the MSE transport in Fig. 6a–c. Solid (dotted) lines denote positive (negative) absolute temperature in degrees Celsius

and colored contours indicate temperature differences between runs/epochs. In Fig. 6d the positive temperature difference in the SH extratropics reflect the warmer SST in Run A. Temperature decreases towards the poles in the extratropics, so the positive temperature difference in the SH of Fig. 6d indicate a reduction in the SH temperature gradient in Run A. Zonal mean available potential energy is transported from the equator towards the poles by the

mean meridional circulation, then converted to eddy available potential energy by baroclinic disturbances, the rate of which depends on the zonal mean temperature gradient (Peixoto and Oort 1991). Therefore, a reduced temperature gradient in Fig. 6d implies a reduction in poleward eddy energy transport, which is manifested in Fig. 6a. A similar relationship between the temperature gradient and the MSE transport difference are exhibited in Fig. 6b, e. Figure 6f shows the temperature difference due to “external forcing”, which is quite distinct from that due to “remote forcing”. There is a warming in the tropics with a maximum at approximately 300 hPa and a cooling in the stratosphere. The situations in the extratropics vary in each hemisphere; in the SH the warming due to the 20C “external forcing” decreases monotonically toward the South Pole, but in the NH there is a cooling centered at 45N due to aerosols, then warming further north. The resulting changes in the temperature gradient are reflected in the MSE transport in Fig. 6c.

4.1.3 Hadley cells and the mean meridional circulation

Now we focus on the mean meridional circulation component of the zonal mean circulation. Figure 7 shows the time-mean, zonally-integrated meridional mass streamfunction for the sets of run(s) and/or epoch(s) identical to those in Fig. 6. The lines and shades denote absolute values and the differences, respectively. The positive difference in the vicinity of the equator in Fig. 7a, c, or a clockwise “anomalous Hadley circulation” (Kang et al. 2009), is due to the strengthening of the northern cell and the widening and hence weakening of the ascending branch in the southern cell, accompanied by the southward shift of the cell boundary. The shift in Fig. 7a is likely to be due to the same mechanism as in Kang et al. (2008, 2009), deducing from the smaller MSE transport by transient eddies in the SH extratropics in the corresponding panels in Fig. 6. In contrast, the shift of the boundary in Fig. 7c may be attributable to the difference between Run A and Epoch A in the SH warming or in upper troposphere warming, hence to the increased tropical static stability as in Mitas and Clement (2006). Both the SH and the upper troposphere warming features are evident in the temperature difference plot in Fig. 6f. In comparison, in Fig. 7b the difference near the equator is small; there is a modest shift of the boundary between the Hadley cells which is southward in the lower troposphere and northward in the upper troposphere.

4.2 Moisture budget

Figure 8a–c is the same as Fig. 6a–c but by the mean meridional circulation. The MSE transport in the lower

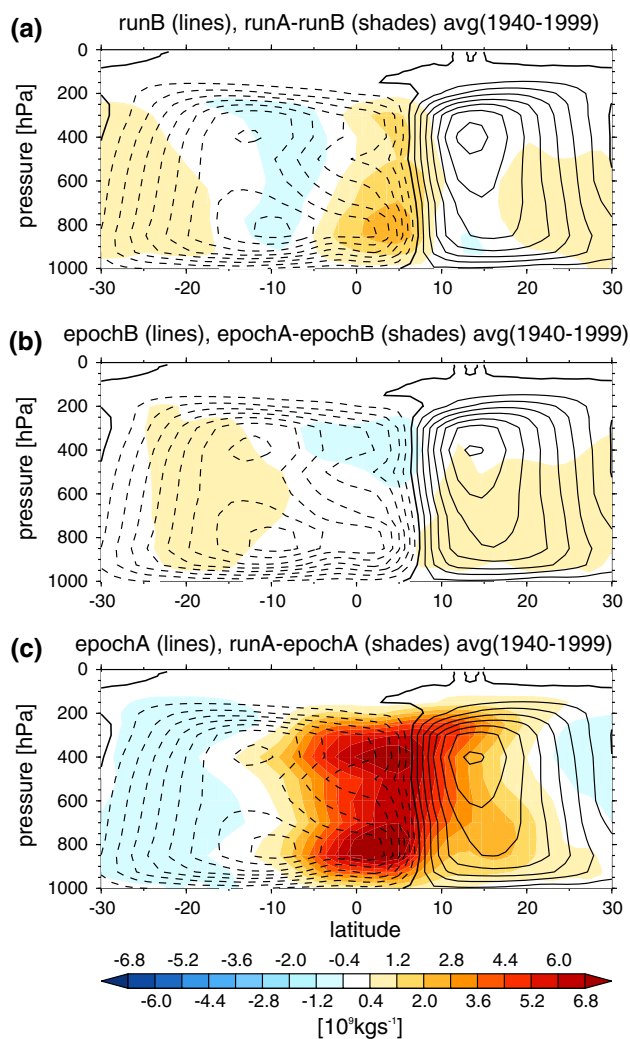
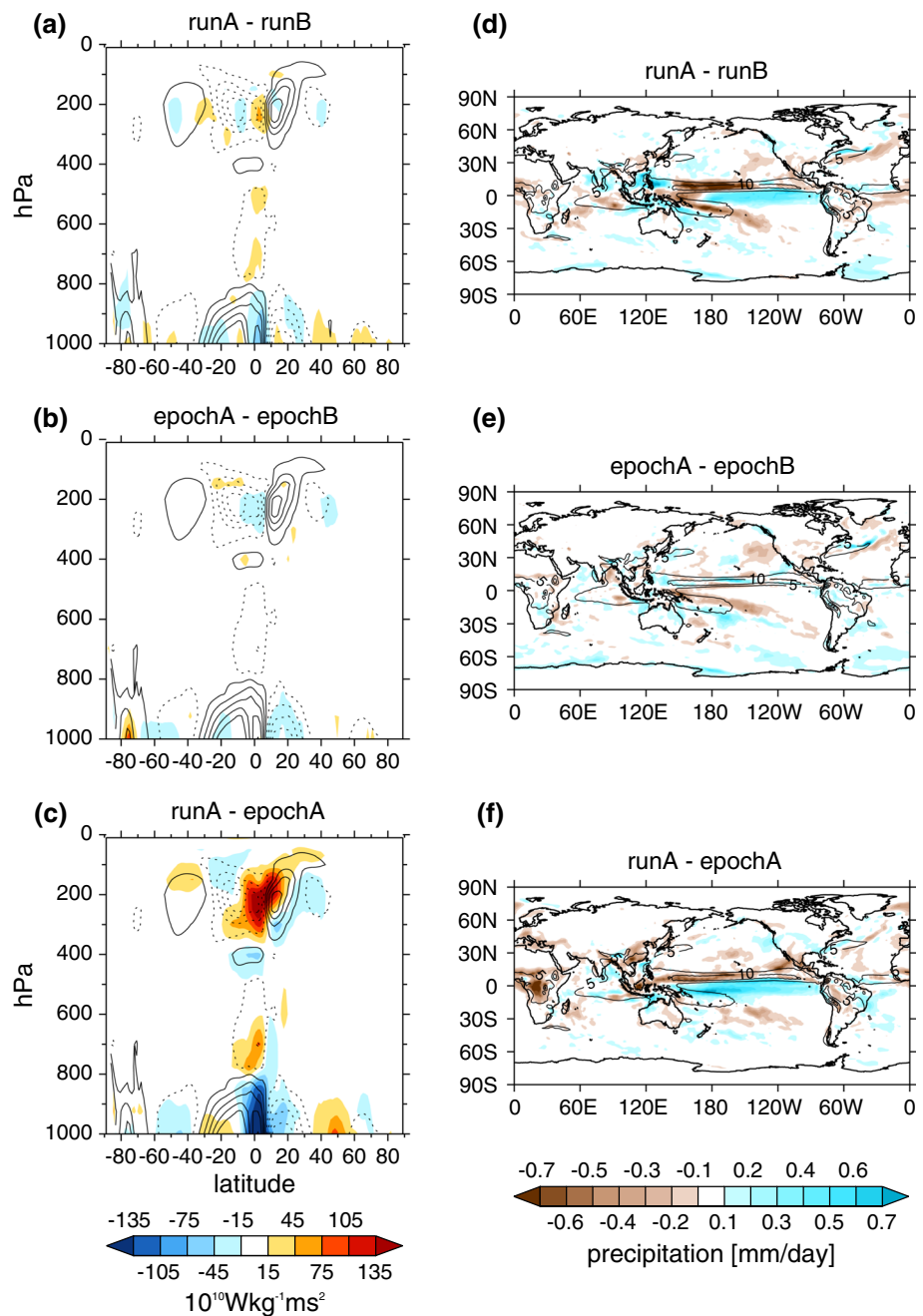


Fig. 7 Time-mean, zonally-integrated meridional streamfunction. The *lines and shades* denote absolute values and the differences, respectively. The *lines* indicate absolute values for Run B (a), Epoch B (b) and Epoch A (c). *Solid (dotted) lines* denote counter-clockwise (clockwise) circulation. The *shades* denote differences between a Run A and Run B, b Epoch A and Epoch B and c Run A and Epoch A. Time average is over the years 1940–1999. Unit is kg s^{-1} . Contour interval of the lines is $6 \times 10^9 \text{ kg s}^{-1}$

branch of the Hadley cell is dominated by water vapor transport $L_v v q$. Therefore, the near-surface differences in Fig. 8a and c indicate that northward water vapor transport to the latitude of the cell boundary near the surface (7N) in Run A, relative to Run B and Epoch A, is reduced.

Figure 8d–f show maps of time-mean precipitation rate differences between runs/epochs. In Fig. 8d, which shows the response to the “remote forcing”, Run A is drier than Run B over the Pacific ITCZ belt straddling 7N. This is due to less water vapor transport from the south and hence less water vapor convergence at the latitude of the ITCZ. This

Fig. 8 Vertical sections of time-mean, zonally-integrated meridional moist static energy transport by mean meridional circulation (a–c) and precipitation averaged over 60 years (d–f). In a–c, solid (dotted) lines denote counter-clockwise (clockwise) circulation of Run B (a), Epoch B (b) and Epoch A (c), respectively. In d–f, solid lines denote the absolute values of Run B (d), Epoch B (e) and Epoch A (f), respectively. Colors denote the differences between Run A and Run B (top), Epoch A and Epoch B (middle) and Run A and Epoch A (bottom), respectively. Time average is over the years 1940–1999. Contour intervals are 5×10^{12} (a–c) and 5 (d–f). Unit is $\text{Wkg}^{-1} \text{ms}^2$ (a–c) and mm day^{-1} (d–f)



feature is associated with a weaker southern Hadley cell in Run A compared with Run B (Fig. 7a) and to a smaller degree to the southward shift in the ITCZ (Fig. 8d). As a result the narrow region to the south of the dry zone between 5S and 5N is wetter in Run A than in Run B, as less water vapor is exported from this region. Figure 8f shows similar characteristics.

We seek to ascertain whether the greater amount of equatorial precipitation observed in Run A is indeed attributable to a greater amount of water vapor convergence and not to less evaporation. The vertically integrated moisture budget can be defined as follows:

$$-\frac{1}{g} \nabla \cdot \int_0^{p_s} vq dp = P - E,$$

where P and E are the rates of precipitation and evaporation per unit area, respectively. Figure 9 shows the time-mean, zonally integrated precipitation (solid line), evaporation (broken line) and the convergence of vertically integrated water vapor transport (dotted line), presented as a difference between Run A and Run B. Latitudes at which the precipitation rates in Run A and Run B differ at the 95 % significance level are shaded. It is clear that in the

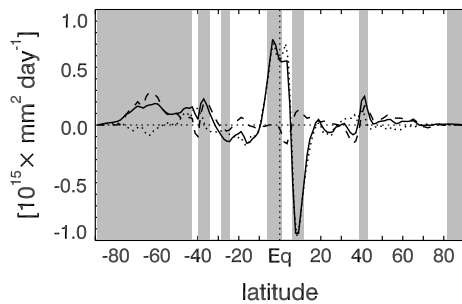


Fig. 9 Time mean, zonally integrated precipitation (*black line*), evaporation (*broken line*) and convergence of vertically integrated water vapor (*dotted line*). Presented as differences between 20C Run A and Run B. Latitudes at which the precipitation rates from Run A and Run B differ at the 95 % significance level are *shaded*. Unit is $10^{15} \text{ mm}^2 \text{ day}^{-1}$

vicinity of the equator the difference in precipitation consists primarily of the difference not in evaporation but in the convergence of transport of water vapor.

It is noted that the actual ITCZ location at approximately 7N as derived from Fig. 8, which is identical to defining ITCZ as the position of maximum zonal mean precipitation, differs from the inferred Hadley cell boundary at 3N, the latitude at which F_A changes sign as seen in Fig. 4b. Some studies also report this discrepancy, the degree of which appears to be model dependent, but the reasons for the discrepancy are not yet clear (Kang et al. 2008).

4.3 Connection between poleward heat transport, ITCZ shift and ENSO amplitude

Watanabe et al. (2012) examined multiple sets of perturbed physics ensembles of CMIP3 and CMIP5 GCMs and found that the amount of precipitation over the eastern equatorial Pacific dictates the strength of ENSO through the shift in the zonal wind stress response to the ENSO SSTA. Figure 10a shows the relationship between the cross-equatorial F_A and the Niño-3 area-mean precipitation for each 20C ensemble member, denoted by colored diamonds. The colors correspond to the degree of warming in the Southern Ocean SST, from blue being the coolest to red being the warmest. The plot clearly shows a monotonic relationship between the amount of cross-equatorial F_A , the Niño-3 area-mean precipitation and the degree of warming in the Southern Ocean SST. This means that members in this ensemble with warmer Southern Ocean SST has a greater amount of precipitation in the Niño-3 region.

Figure 10b shows the relationship between the Niño-3 area-mean precipitation and the ENSO amplitude, σ . The black dots denote 156-year mean values in CTL. There is a systematic quasi-linear relationship between the two quantities in both CTL and 20C, which agrees with the findings in Watanabe et al. (2012), that in the eastern

equatorial Pacific a strong relationship exists between the amount of precipitation and the strength of ENSO. Thus we argue that at least part of the ENSO diversity is attributable to the change in equatorial Pacific precipitation. This change in precipitation resulted from a change in the Hadley circulation, which in turn was caused by reduced southward heat transport by transient eddies. The southward heat transport was diminished because the equator-to-pole temperature gradient in the SH had decreased due to the warming of the Southern Ocean.

There remains a possibility that the greater amount of equatorial precipitation in the warmer ensemble members may simply be a result of the warmer equatorial mean SST. To quantify the relative contributions of the processes affecting precipitation in this region, we apply to our 20C ensemble a method proposed by Watanabe and Wittenberg (2012) to separate out the effects of the ENSO cycle and the background mean SST on the mean precipitation in the eastern equatorial Pacific. Figure 11 decomposes the change in the mean precipitation in the Niño-3 region into four factors, namely the effect of change in the sensitivity of precipitation to SST, the effect of change in the ENSO amplitude, the effect of change in the mean SST and the nonlinear impacts on mean precipitation. It is found that the effect of change in the sensitivity of precipitation to SST (cyan), which arises from the change in the atmospheric circulation since the change in static stability ($\sim \partial T / \partial p$) is small as seen in Fig. 6d, accounts for approximately a third of the total, whilst the changes in the ENSO amplitude feedback (red) and mean SST (orange) account for the rest. This suggests that although the main causes of the greater amount of equatorial precipitation in the ensemble members with warmer Southern Ocean SST are indeed changes in mean SST and ENSO amplitude in the equatorial Pacific, the change deriving from a series of events associated with anomalously warm Southern Ocean SST is also a substantial source. We conclude that in this GCM, there is an energy pathway, as described above, that indeed in part accounts for diversity in the ENSO strength. Its contribution to the diversity of ENSO strength may not be dominant, but there is no doubt this pathway exists; otherwise the ENSO strengths in the ensemble would not vary so systematically.

5 Summary and discussion

In this paper we analyzed key physical properties from the CMIP5 historical transient and pre-industrial control experiments conducted with the MIROC5 coupled atmosphere–ocean GCM to investigate why the ENSO was stronger in members of the historical ensemble with warmer Southern Ocean SST. We suggest this resulted in part from the following sequence of events:

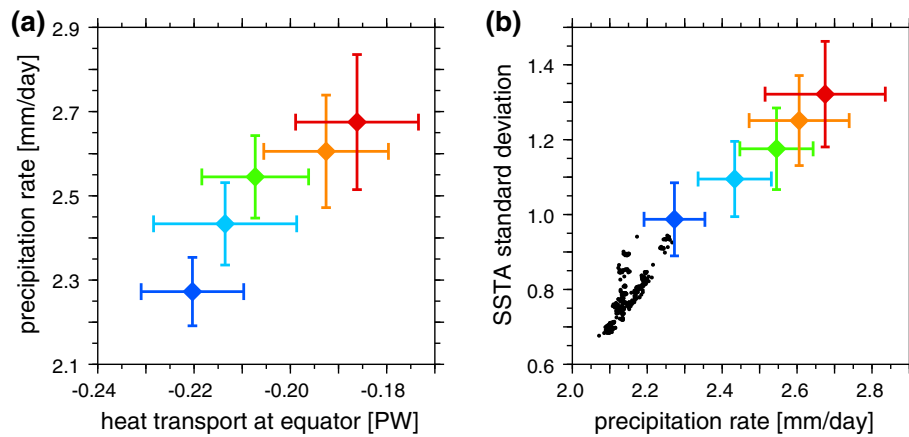


Fig. 10 **a** Scatter plot of time mean, zonally-integrated meridional heat transport (in petawatts) at the equator against the standard deviation of Niño-3 area-mean SSTA (σ , in K) computed over the 1940–1999 period for the 20C ensemble members. **b** Scatter plot of time mean, Niño-3 area-mean precipitation rate (in mm day^{-1}) against σ , computed over the 1940–1999 period for the 20C ensemble members (colored diamonds) and over 156-year subsets of CTL

(black dots). Colors correspond to the degree of the warming of the Southern Ocean SST in each 20C ensemble member, from blue being the coolest to red being the warmest. Error bars represent ranges of standard deviations (for σ) and means (for precipitation and heat transport), which were obtained from ninety-six 60-year subsets within the 1940–1999 period. The subsets were generated by repeatedly shifting the years included in a subset forward by 1 year

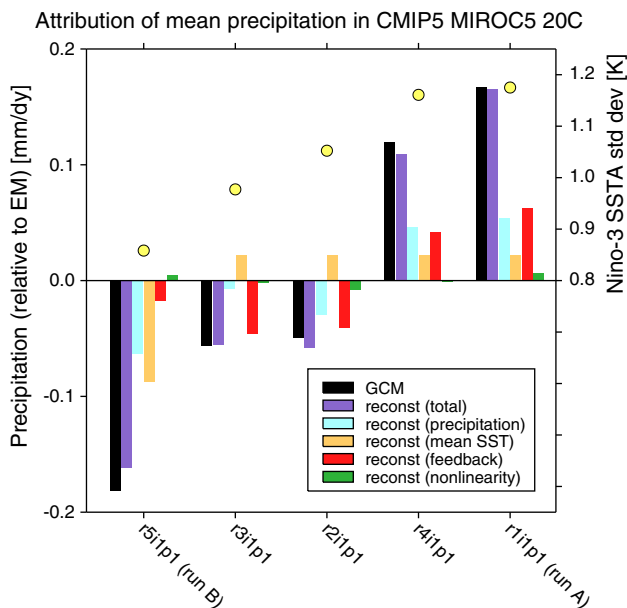


Fig. 11 Reconstruction of mean Niño-3 precipitation for the 20C ensemble, minus ensemble mean. Black and purple bars denote total change in mean precipitation obtained from direct GCM output and from reconstruction, respectively. Bars in the following colors indicate different factors comprising the change in the mean precipitation. Light blue effect of change in the sensitivity of precipitation to SST, orange effect of change in mean SST, red effect of change in ENSO amplitude, green nonlinear impacts on mean precipitation. Yellow circles denote standard deviation of Niño-3 SSTA anomaly

1. Excess heat flux from positive TOA radiative imbalance enters and heats up the global ocean. Ocean transports positive heat southwards into the Southern Ocean. Southern Ocean SST is increased.

2. Extratropical warming in the Southern Ocean SST reduces the equator-to-pole atmospheric temperature gradient. Baroclinic instability in the extratropics becomes weaker and/or less frequent. Less heat is transported by transient eddies from the tropics to the extratropics. To maintain energy balance on both sides of the division of the Hadley cells, mass transport within the Hadley cells change (decreases in the southern cell and modestly increases in the northern cell) and the position of the cells and their divisional boundary, which corresponds to the ITCZ near the surface, shift southward. Anomalous southward water vapor transport in the deep tropics increases. Precipitation in the Niño-3 region increases.
3. ENSO amplitude in the Niño-3 region increases.

It is possible that other factors may also come into play. For instance, there is a possibility that it is the strong ENSO that warmed the Southern Ocean and not the converse. As an example of such a case, by conducting a numerical experiment with an atmospheric GCM coupled to a slab-ocean with imposed heat flux anomaly over the tropical Pacific Ocean to induce an El Niño-like SST anomaly in the equatorial Pacific, Li (2000) reproduced a Southern Ocean SST anomaly pattern similar to one found in a regression coefficient map obtained by regressing observed SST onto the Niño-3 index. Li (2000) concludes that the SST anomaly in the tropical Pacific influenced the SST in the Southern Ocean through atmospheric teleconnection, i.e. through changes in the atmospheric circulation that led to changes in the air-sea heat flux, which altered the Southern Ocean SST. Although it is an entirely possible

scenario, it is not likely to have been the dominant process causing the anomalously warm Southern Ocean SST found in our ensemble, as the sign of the area-averaged, annual-mean net surface heat flux into the ocean in this region is negative throughout the 156 years. Negative net heat flux into the ocean means that the atmosphere cools the ocean (or the ocean warms the atmosphere), so the mechanism suggested in Li (2000) does not apply to our ensemble. Indeed, we found instead that the heating of the Southern Ocean was due to a positive time-mean, longitude-depth-section-mean southward heat transport by the ocean, the amount of which at 50S was approximately 0.4 PW.

Another possibility can be raised that it may be the ocean that transported the anomalous heat northward from the SH extratropics to the tropics. This scenario, however, can also be negated, as far as net heat is concerned, for the reason given above that the mean meridional ocean heat transport across 50S is 0.4 PW southwards.

In terms of ocean physics, changes to ENSO amplitudes may be expressed as the SSTA tendency in the equatorial Pacific region, which can be broken down into effects from advection (including upwelling), diffusion, surface heat flux, mixed-layer physics and convection. Each term depends on one or more of the following: ocean circulation, temperature, temperature gradient and density stratification. Therefore, changes in the ocean state might also play an important role, although upwelling and mixed-layer physics are also strongly tied to surface winds.

Yet another possibility is that the greater amount of equatorial precipitation in the warmer ensemble members may simply be a result of the warmer equatorial mean SST. Following the method of Watanabe and Wittenberg (2012) we separated out the effects of the ENSO cycle and the background mean SST on the mean precipitation in the eastern equatorial Pacific. It is found that the effect of change in the sensitivity of precipitation to SST, which arose from the change in the atmospheric circulation, accounts for approximately a third of the total. This suggests that although the main causes of the greater amount of equatorial precipitation in the ensemble members with warmer Southern Ocean SST are indeed changes in mean SST and ENSO amplitude in the equatorial Pacific, the change deriving from a series of events associated with anomalously warm Southern Ocean SST is also a substantial source.

Why does the excess heat end up in the Southern Ocean in this ensemble? In equilibrium, in an annual mean sense, the net heat loss at the surface of the Southern Ocean would be compensated by the positive southward net ocean heat transport into the region, keeping the mean Southern Ocean SST constant (with internal variability). With that in mind, the reason the excess heat has ended up in the Southern Ocean may be twofold—one direct and the other indirect. The first, direct cause may be the continual melting of sea

ice in the Southern Ocean throughout CTL. The diminution in sea ice cover has led to an increase in the absorption of shortwave radiation and upwelling of warm subsurface water, and hence the warming of near-surface ocean temperature. The presence of sea ice makes this a positive feedback because the warming would further induce the sea ice melt. On the other hand, a higher SST would cause the outgoing longwave, latent and sensible heat fluxes to increase, which would work to damp the SST warming, but in the present case the balance appears to be such that the SST increases steadily. The reason why the sea ice had begun to melt in the first place, however, is unclear.

The second, indirect cause may be a consequence of the global thermohaline circulation. The excess heat from the TOA imbalance enters the ocean, sinks and is transported southward by the overturning circulation into the Southern Ocean and upwells, thereby warming the upper Southern Ocean. It is noted that although there are changes to the amount of heat transported by the overturning circulation, there is little change in the overturning mass streamfunction itself.

The perpetual interaction between the mean climate state and ENSO plays a vital role in the dynamics of ENSO and should not under any circumstances be underemphasized (Wittenberg 2009). This notwithstanding, in this paper the importance of remote forcing in modulating the strength of ENSO has been demonstrated. The CMIP5 models currently exhibit a large diversity in ENSO strength (Guilyardi et al. 2012; Bellenger et al. 2013). There is a possibility that the model-dependent ENSO strength at present may benefit from improving the model physics and dynamics relating to the Southern Ocean.

Acknowledgments We would like to thank Fei-Fei Jin, Noel Keenlyside and Arnaud Czaja for their helpful discussions. We are grateful to the two reviewers for their insightful and constructive comments. Hiroaki Tatebe, Tatsuo Suzuki, Yoshiki Komuro and Takao Kawasaki gave us valuable advice on ocean surface flux data analysis. We acknowledge the World Climate Research Programme's Working Group on Coupled Modelling, which is responsible for CMIP, and we thank the climate modeling groups (listed in Table 1 of this paper) for producing and making available their model output. For CMIP the U.S. Department of Energy's Program for Climate Model Diagnosis and Intercomparison provides coordinating support and led development of software infrastructure in partnership with the Global Organization for Earth System Science Portals.

Open Access This article is distributed under the terms of the Creative Commons Attribution License which permits any use, distribution, and reproduction in any medium, provided the original author(s) and the source are credited.

Appendix

Individual terms displayed in Fig. 3a were calculated offline as follows.

Δ Planck feedback: T_s^4 ,
 Δ clear-sky water vapor GH forcing: $T_s^4 - \Delta$ clear-sky flux
of longwave radiation at TOA,
 Δ total cloud radiative forcing: Δ clear-sky flux of long-
wave radiation at TOA

- Δ total flux of longwave radiation at TOA
- + Δ clear-sky flux of shortwave radiation at TOA
- Δ total flux of shortwave radiation at TOA,

effect of change in surface albedo: Δ clear-sky shortwave
wave forcing at TOA,

$\Delta(\nabla \cdot F_A)$: Δ Net downward radiation at TOA – Δ net
heat into surface,

ΔF_s : Δ net heat into surface,

where σ is the Stefan–Boltzmann constant and T_s is surface
temperature.

References

- Bellenger H, Guilyardi E, Leloup J, Lengaigne M, Vialard J (2013) ENSO representation in climate models: from CMIP3 to CMIP5. *Clim Dyn* 42(7–8):1999–2018. doi:10.1007/s00382-013-1783-z
- Broccoli AJ, Dahl KA, Stouffer RJ (2006) Response of the ITCZ to northern hemisphere cooling. *Geophys Res Lett* 33(1). doi:10.1029/2005GL024546
- Chiang JCH, Bitz CM (2005) Influence of high latitude ice cover on the marine intertropical convergence zone. *Clim Dyn* 25(5):477–496. doi:10.1007/s00382-005-0040-5
- Collins M, An SI, Cai W, Ganachaud A, Guilyardi E, Jin FF, Jochum M, Lengaigne M, Power S, Timmermann A, Vecchi G, Wittenberg A (2010) The impact of global warming on the tropical Pacific Ocean and El Niño. *Nat Geosci* 3:391–397. doi:10.1038/NGEO868
- Frierson DMW, Hwang YT (2012) Extratropical influence on ITCZ shifts in slab ocean simulations of global warming. *J Clim* 25(2):720–733. doi:10.1175/JCLI-D-11-00116.1
- Gastineau G, Le Treut H, Li L (2008) Hadley circulation changes under global warming conditions indicated by coupled climate models. *Tellus A* 60(5):863–884. doi:10.1111/j.1600-0870.2008.00344.x
- Gregory JM, Mitchell JFB (1997) The climate response to CO2 of the Hadley Centre coupled AOGCM with and without flux adjustment. *Geophys Res Lett* 24(15):1943–1946. doi:10.1029/97GL01930
- Guilyardi E, Bellenger H, Collins M, Ferret S, Cai W, Wittenberg A (2012) A first look at ENSO in CMIP5. *Clivar Exch* 58:29–32. doi:10.1029/2009PA001892
- Gupta AS, Jourdain NC, Brown JN, Monselesan D (2013) Climate drift in the CMIP5 models. *J Clim* 26(21):8597–8615. doi:10.1175/JCLI-D-12-00521.1
- Halpert MS, Ropelewski C (1992) Surface temperature patterns associated with the Southern Oscillation. *J Clim* 5(6):577–593. doi:10.1175/1520-0442(1992)005<0577:STPAWT>2.0.CO;2
- Hasumi H (2006) CCSR Ocean Component Model (COCO), version 4.0. Tech. rep., Center for Climate System Research Rep. <http://ccsr.aori.u-tokyo.ac.jp/~hasumi/COCO/coco4.pdf>
- Kang SM, Held IM, Frierson DMW, Zhao M (2008) The response of the ITCZ to extratropical thermal forcing: idealized slab-ocean experiments with a GCM. *J Clim* 21(14):3521–3532. doi:10.1175/2007JCLI2146.1
- Kang SM, Frierson DMW, Held IM (2009) The tropical response to extratropical thermal forcing in an idealized GCM: the importance of radiative feedbacks and convective parameterization. *J Atmos Sci* 66(9):2812–2827. doi:10.1175/2009JAS2924.1
- Kang SM, Polvani LM, Fyfe JC, Sigmond M (2011) Impact of polar ozone depletion on subtropical precipitation. *Science* 332(6032):951–954. doi:10.1126/science.1202131
- Klingaman NP (2009) Climate laboratory notes. Second UJCC-NCAS Climate Modelling Summer School, September 11, 2009
- Li ZX (2000) Influence of tropical Pacific El Niño on the SST of the Southern Ocean through atmospheric bridge. *Geophys Res Lett* 27(21):3505–3508. doi:10.1029/1999GL011182
- Lu J, Vecchi GA, Reichler T (2007) Expansion of the Hadley cell under global warming. *Geophys Res Lett* 34(6). doi:10.1029/2006GL028443
- Meehl GA, Covey C, Delworth T, Latif M, McAvaney B, Mitchell JFB, Stouffer RJ, Taylor KE (2007) The WCRP CMIP3 multi-model dataset: a new era in climate change research. *Bull Am Meteorol Soc* 88(9):1383–1394
- Menviel L, Timmerman A, Timm OE, Mouchet A (2010) Climate and biogeochemical response to a rapid melting of the West Antarctic Ice Sheet during interglacials and implications for future climate. *Paleoceanography* 25(4). doi:10.1029/2009PA001892
- Mitas CM, Clement A (2006) Recent behavior of the Hadley cell and tropical thermodynamics in climate models and reanalyses. *Geophys Res Lett* 33(1). doi:10.1029/2005GL024406
- Peixoto JP, Oort AH (1991) *Physics of climate*. Springer, Berlin
- Rayner NA, Parker DE, Horton EB, Folland CK, Alexander LV, Rowell DP, Kent EC, Kaplan A (2003) Global analyses of sea surface temperature, sea ice, and night marine air temperature since the late nineteenth century. *J Geophys Res* 108(D14). doi:10.1029/2002JD002670
- Ropelewski C, Halpert MS (1987) Global and regional scale precipitation associated with El Niño/Southern Oscillation. *Mon Weather Rev* 115(8):1606–1626. doi:10.1175/1520-0493(1987)115<1606:GARSPP>2.0.CO;2
- Ropelewski C, Halpert MS (1989) Precipitation patterns associated with the high index phase of the Southern Oscillation. *J Clim* 2(3):268–284. doi:10.1175/1520-0442(1989)002<0268:PPAWTH>2.0.CO;2
- Su J, Wang H, Yang H, Drange H, Gao Y, Bentsen M (2008) Role of the atmospheric and oceanic circulations in the tropical Pacific SST changes. *J Clim* 21(10):2019–2034. doi:10.1175/2007/JCL1692.1
- Taylor KE, Stouffer R, Meehl G (2012) An overview of CMIP5 and the experiment design. *Bull Am Meteorol Soc* 93(4):485–498. doi:10.1175/BAMS-D-11-00094.1
- Trenberth KE, Solomon A (1994) The global heat balance: heat transports in the atmosphere and ocean. *Clim Dyn* 10(3):107–134. doi:10.1007/BF00210625
- Watanabe M, Wittenberg AT (2012) A method for disentangling El Niño-mean state interaction. *Geophys Res Lett* 39(14). doi:10.1029/2012GL052013
- Watanabe M, Suzuki T, Oishi R, Komuro Y, Watanabe S, Emori S, Takemura T, Chikira M, Ogura T, Sekiguchi M, Takata K, Yamazaki D, Yokohata T, Nozawa T, Hasumi H, Tatebe H, Kimoto M (2010) Improved climate simulation by MIROC5: mean states, variability, and climate sensitivity. *J Clim* 23(23):6312–6335. doi:10.1175/2010JCLI3679.1
- Watanabe M, Kug JS, Jin FF, Collins M, Ohba M, Wittenberg AT (2012) Uncertainty in the ENSO amplitude change from the past

- to the future. *Geophys Res Lett* 39(20). doi:[10.1029/2012GL053305](https://doi.org/10.1029/2012GL053305)
- Wittenberg AT (2009) Are historical records sufficient to constrain ENSO simulations? *Geophys Res Lett* 36(12). doi:[10.1029/2009GL038710](https://doi.org/10.1029/2009GL038710)
- Yoshimori M, Broccoli AJ (2009) On the link between Hadley circulation changes and radiative feedback processes. *Geophys Res Lett* 36(20). doi:[10.1029/2009GL040488](https://doi.org/10.1029/2009GL040488)